The amorphization of 3C-SiC irradiated at moderately elevated temperatures as revealed by X-ray diffraction

Alexandre Boulle, A. Debelle, J.B. Wallace, L.B. Bayu Aji, L B Bayu Aji, S.O. O Kucheyev

▶ To cite this version:

Alexandre Boulle, A. Debelle, J.B. Wallace, L.B. Bayu Aji, L B Bayu Aji, et al.. The amorphization of 3C-SiC irradiated at moderately elevated temperatures as revealed by X-ray diffraction. Acta Materialia, 2017, 140, pp.250-257. 10.1016/j.actamat.2017.08.030 . hal-02193096

HAL Id: hal-02193096
https://hal.science/hal-02193096v1

The amorphization of 3C-SiC irradiated at moderately elevated temperatures as revealed by X-ray diffraction

A. Boulle[1], A. Debelle[2], J. B. Wallace[3,4], L. B. Bayu Aji[3], and S. O. Kucheyev[3]

[1] Science des Procédés Céramiques et Traitements de Surface, CNRS UMR 7315, Centre Européen de la Céramique, 12 rue Atlantis, 87068 Limoges, France.

[2] Centre de Sciences Nucléaires et de Sciences de la Matière, Université Paris-Sud, CNRS/IN2P3, Université Paris-Saclay 91405 Orsay, France.

[3] Lawrence Livermore National Laboratory, Livermore, CA 94550, USA

[4] Department of Nuclear Engineering, Texas A&M University, College Station, TX 77843, USA

Abstract

Mechanisms of radiation damage buildup in 3C-SiC remain poorly understood. Here, we use X-ray diffraction in combination with numerical simulations to study depth profiles of radiation-produced strain and lattice damage in 3C-SiC bombarded in the temperature range of 25-200 °C with 500 keV Ar ions. Results reveal increased defect recombination with increasing temperature, with a critical amorphization fluence increasing from 0.17 to 0.44 displacements per atom. The amorphization process is found to be correlated with the evolution of lattice strain. We find that, at fluences corresponding to the onset of amorphization, lattice strain is ~2% and is independent of temperature. With continuing bombardment above the onset of amorphization, the strain in the crystal bulk increases and reaches a saturation value that decreases from 7% to 5% with increasing temperature. Based on strain profiles, we compute depth profiles of the effective concentration of point defect clusters in the crystalline phase. Bombardment at higher temperatures results in lower maximum defect concentrations pointing to enhanced defect mobility.

1. Introduction

Silicon carbide (SiC) exhibits interesting electronic and structural properties, which makes it an important material for both electronic and nuclear applications [1, 2, 3, 4]. For both applications, the understanding of radiation-induced damage is highly desirable. This has motivated a large number of both theoretical and experimental studies in the last decades [3, 5, 6, 7, 8, 9, 10, 11, 12, 13, 14, 15, 16]. Material's resistance to amorphization has been of particular interest in previous studies of damage build-up in SiC (*i.e.,* disorder *vs.* ion fluence). It has now been well established for all the three major polytypes of SiC (3C, 6H, and 4H) that the amorphization process is delayed or even completely suppressed with increasing sample temperature [7, 8]. The threshold temperature above which amorphization no longer occurs lies in the 200-400 °C range, depending on irradiation conditions such as mass, energy, the nature (*i.e.*, chemistry), and the dose rate of bombarding ions.

The present study focuses on radiation effects in the cubic (3C) polytype of SiC, which is of particular interest to nuclear technologies [1, 3]. Previous studies of the temperature dependence of damage buildup in 3C-SiC are scarce. From an experimental standpoint, apart from reports focused on the specific case of He-ion-induced damage in SiC [17, 18], one can cite systematic studies reported by Weber *et al.* [8] as well as by some of the present authors [19]. In both of these studies [8, 19], the level of damage was quantitatively determined by Rutherford backscattering spectrometry in channeling mode (RBS/C). Both works provided evidence that, even at moderate temperatures of 250 °C and below, 3C-SiC undergoes pronounced dynamic annealing involving enhanced defect recombination. Furthermore, in Ref. [19], a comprehensive analysis of RBS/C-derived depth profiles of disorder revealed anomalous features and pointed out to the crucial importance of radiation defect dynamics, as also confirmed in two other studies [20, 21].

A recent investigation by a combination of X-ray diffraction (XRD) experiments and molecular dynamics (MD) simulations has suggested that the relieve of the elastic energy associated with the strain induced by small point defect clusters is the main driving force for amorphization of 3C-SiC [22]. In addition to the damage level, the determination of the strain level is, therefore, an important aspect in the understanding of the radiation resistance of 3C-SiC. That previous work by Debelle and coworkers [22] was, however, limited to bombardment at room-temperature (RT, ~25 °C). In the present work, we use XRD to study damage buildup in 3C-SiC bombarded at moderately elevated temperatures (25-200 °C) with 500 keV Ar ions. Numerical simulations [23, 24] of XRD data allow us to retrieve depth-profiles of both lattice strain and damage and to compare them with the damage profiles previously measured by RBS/C [19]. In agreement with previous RBS/C studies [19], we find that dynamic annealing is enhanced with increasing sample temperature, even at these moderate temperatures, requiring higher ion fluences to reach amorphization. More importantly, the fluence- and temperature-dependent behavior of XRD-derived strain depth profiles suggests that the elastic energy associated with stable point defect clusters controls the amorphization process in SiC in the entire temperature range. Based on the strain profiles, we compute depth-profiles of the concentration of stable point defect clusters. The computed defect concentrations reveal a higher defect recombination rate with increasing temperature.

2. Experimental details

2.1 Irradiation

In this work, we studied epitaxial films of (001)-oriented 3C-SiC (grown on Si substrates) obtained from NOVASiC. The films had a thickness (*t*) of ~2 µm. To improve thermal contact during irradiation, the samples were attached to a Ni sample holder with silver paste. Films were irradiated at 25, 100, and 200 °C (with a temperature accuracy of ±1 °C) with 500 keV Ar^+ ions at 7° off the [001] direction to minimize channeling effects. For each temperature, the ion fluences used are summarized in Table I. An instantaneous dose rate of $(1.9\pm0.1)\times10^{13}$ cm^{-2} s^{-1} was kept constant in all the runs. Additional details of the irradiation conditions used can be found in a previous work [19].

2.2 X-ray diffraction

Post-irradiation XRD analysis was performed with a Cu Kα_1 x-ray source (wavelength λ = 1.5406 Å) on a Bruker D8 Discover diffractometer equipped with a parabolic multilayer mirror and a two-reflection asymmetrically cut Ge(220) monochromator as primary optics and a linear position sensitive detector covering a 2° 2θ-range with a 0.01° angular resolution. Symmetrical high-resolution θ-2θ scans were performed by selecting a single channel of the detector. The 002 reflection of SiC ($2\theta_B$ = 41.394°) was scanned, with 0.005° steps, over a 2θ range wide enough to include all the diffraction signal coming from the irradiated region. Symmetrical θ-2θ scans probe the reciprocal space in the direction normal to the film surface and are, therefore, sensitive to both the film thickness and the level of strain and damage in the film. When a reflection corresponding to lattice planes parallel to the surface is selected (*i.e.,* any 00*l* reflection for a (001)-oriented crystal), the XRD curves reflect only the e_{zz} component of the strain tensor, where the *z* direction is normal to the surface of 3C-SiC.

2.3 Determination of strain and damage depth-profiles

The XRD curves were numerically simulated with the RaDMaX program [25] in order to determine depth-resolved strain and damage profiles. The underlying principles of simulation procedure are briefly recalled below, and additional details can be found in previous publications [23, 25].

In the presence of atomic displacements, characterized by a vector **u**, the diffracted amplitude from the irradiated region, recorded around the reflection with reciprocal vector **h**, can be written as [26]:

$$E(\mathbf{Q})=F(Q)\int_V d^3\mathbf{r}\cdot\exp[i\mathbf{Q}\cdot\mathbf{u}(\mathbf{r})]\exp[i(\mathbf{Q}-\mathbf{h})\cdot\mathbf{r}] \quad , \qquad (1)$$

where the integration is performed over the volume irradiated by the X-ray beam, *F* is the structure factor, **r** (with components *x*, *y*, *z*) is the spatial coordinate within the damaged region, **Q** is the scattering vector (with modulus **Q** = 4 π sinθ / λ). As mentioned in Sec. 2.2, for a (001)-oriented crystal, the measurement of a 00*l* reflection actually selects the *z*-component of the displacement field and, since the single crystal is laterally infinite as compared to the X-ray wavelength, the problem reduces to the following one-dimensional integral:

$$E(Q_z)=F(Q_z)\int_0^{t_{irr}} dz\cdot\exp\left[iQ_z\cdot u_z(z)\right]\exp\left[i(Q_z-h_z)\cdot z\right] \quad . \tag{2}$$

From a phenomenological point of view, irradiation damage produces two type of atomic displacements: random displacements, δ**u(r)**, and correlated displacements, **e(***z***).r**, where **e**(*z*) is the strain tensor. The strain tensor depends on the out-of-plane coordinate, *z*, since, in irradiated materials, the variation of lattice strain is confined along the out-of-plane direction [23]. The displacement vector reads:

$$\mathbf{u}(\mathbf{r})=\delta\mathbf{u}(\mathbf{r})+\mathbf{e}(z)\cdot\mathbf{r} \quad . \tag{3}$$

The amplitude scattered from the sample is, therefore, the result of the average over the random variable δ**u(r),** and the coherent diffraction intensity is the squared modulus of the amplitude, so that:

$$I(Q_z)=\left|F(Q_z)\int_0^{t_{irr}} dz\cdot\left\langle\exp\left[iQ_z\cdot\delta u_z(z)\right]\right\rangle\exp\left[iQ_z\cdot e_{zz}\cdot z\right]\exp\left[i(Q_z-h_z)\cdot z\right]\right|^2 \quad . \tag{4}$$

The brackets <.> indicate the average over the *x,y* coordinates and the corresponding term is the static Debye-Waller (DW) factor, which yields a lowering of the diffracted amplitude [26]. The second exponential, containing the e_{zz} strain component, yields a shift of the XRD peak. Equation (4) shows that the analysis of the diffracted intensity distribution allows to determine (i) the depth-resolved strain profile, $e_{zz}(z)$, and (ii) the depth-resolved damage profile quantified by the DW factor. In the following, the damage is defined as 1 – DW, which lies in the [0,1] range, where 0 corresponds to a perfect crystal, and 1 corresponds to a fully damaged crystal. It should be noted that the DW factor, and, hence, the corresponding damage value, is a function of Q_z and it is, therefore, not an absolute measure of lattice damage [24]. Instead, it provides a convenient quantitative comparison of lattice damage in different samples, provided that the same lattice planes are probed in the XRD experiment.

In equation (4) the integral runs from 0 to t_{irr}, which is the irradiated thickness. The intensity recorded in an actual experiment also includes the diffraction from the pristine region below the irradiated region. In the present case, diffraction from the pristine region actually corresponds to diffraction from a SiC film with amplitude E^0_{SiC} (on a Si substrate) with finite thickness $t - t_{\mathrm{irr}}$. In the case of the 002 reflection, there is no diffraction from the underlying Si substrate since this reflection is forbidden ($E^0_{\mathrm{Si}} = 0$). The diffraction geometry is schematically represented in Fig. 1.

The RaDMaX program [25], initially developed to analyze bulk single-crystals, was modified to include the film/substrate geometry corresponding to the samples studied in the present work. Moreover, in order to correctly account for the diffraction from thick crystals, the implementation was performed within the dynamical theory of diffraction [23,25]. Within this theory, the diffraction equation is solved recursively by dividing the irradiated regions in thin lamellas, within which the strain and damage are constant. As schematically represented in Fig. 1, each lamella scatters a sub-part of the overall diffracted amplitude. In the present work, 60 lamellas, each with a thickness of 10 nm, were used for the simulations, so that the accuracy of the depth location is not better than 10 nm.

Another important specificity of epitaxial 3C-SiC layers comes from the large lattice mismatch of 3C-SiC and Si (19.7%), which causes stacking faults and associated Shockley dislocations to form at the SiC/Si interface [27]. The presence of stacking faults in our films is indeed confirmed by the existence of scattering streaks making an angle of 54.7° with respect to the [001] direction (data not shown here), forming a characteristic star-like pattern in the reciprocal space [28]. The associated Shockley partial dislocations generate lattice distortions which contribute to the broadening of XRD curves [29]. Because of the limited film thickness, these distortions also affect the irradiated region. In the simulations presented here, this effect was accounted for by the convolution of the calculated curves with a pseudo-Voigt function (*i.e.,* a linear combination of Gaussian and Lorentzian functions) with a 0.03° full-width at half-maximum and 15% Lorentzian content. These values were found to be constant for all the samples studied, independent of irradiation conditions, and, therefore, will not be discussed any further.

3. Results

Figures 2(a), 2(b), and 2(c) show experimental and simulated θ-2θ scans from 3C-SiC samples irradiated to different fluences at 25, 100, and 200 °C, respectively. The most intense peak located at 41.394° corresponds to the signal coming from the pristine (unirradiated) 3C-SiC, indicating that the penetration depth of the X-ray beam is larger than the thickness damaged by Ar ion bombardment. This is not unexpected since, for the 002 angular setting, the attenuation length of CuKα_1 X-rays in 3C-SiC is ~25 μm, which is indeed much larger than the projected range of 500 keV Ar ions in 3C-SiC (~ 350 nm).

In Figs. 2(a)-2(c), the broad signal at lower 2θ angles originates from the near-surface region with ion-beam-induced damage. The fact that such a signal is at lower 2θ angles indicates the presence of a damage-induced dilatation gradient in the direction normal to the sample surface [12]. It is also seen from Fig. 2 that, at all three temperatures, with increasing fluence, this dilatation-related signal extends to lower angles, indicating an increase in the level of tensile strain. In addition to extending to lower angles, the damage-related signal intensity rapidly decreases with increasing fluence, indicating an increase in the level of lattice damage [17, 22, 24].

As mentioned in the previous section, depth-profiles of both lattice strain and damage can be obtained by the simulation of XRD curves such as shown in Fig. 2. Such simulated XRD curves are shown as solid lines in Fig. 2. For all the cases studied, a relatively good fit of simulated curves to experimental data was obtained. Figure 3 shows the strain (3a, 3c, 3e) and damage (3b, 3d, 3e) depth-profiles obtained from the simulation of XRD curves for the three temperatures studied.

Let us first discuss strain depth profiles from Fig. 3(a) for the 25 °C case. These profiles are bellshaped, only slightly asymmetric, with a maximum strain located at ~290 nm, extending down to ~550 nm from the sample surface. With increasing fluence, the level of strain increases monotonically, while the position of the strain maximum remains unchanged. Given the accuracy of the XRD depth determination (~10 nm), these observations are in excellent agreement with the damage profiles obtained by RBS/C for the same set of samples [19] as well as with TRIM simulations (see [19] for details) which predict the maximum of ballistically generated displacements around ~300 nm below the surface. Figure 3(a) also shows that, for the highest fluence used at 25 °C (5×10^{14} cm^{-2}), the maximum strain reaches 7%, which is in agreement with values reported in a recent short review on this topic [16].

Regarding the damage profiles for the 25 °C case [Fig. 3(b)], the first observation is that they exhibit a much less regular shape than the corresponding strain profiles from Fig. 3(a). This is actually a rather general feature of XRD-derived damage values, which turn out to be much less robust than strain profiles, especially when the XRD signal does not exhibit pronounced interference features, as it is the case here (see Fig. 2). This larger uncertainty reduces the accuracy in the determination of the depth of the damage peak. The damage peak is found to be in the 300-340 nm range, which is deeper than the depth of peaks in strain profiles [Fig. 3(a)], RBS/C-derived damage profiles, and TRIM-predicted distribution of the ballistically-generated vacancies [19]. However, because of the aforementioned accuracy degradation, this discrepancy is more likely to be due to the uncertainty inherent to the XRD simulation than to a any physical reason.

Figure 3(b) also shows a progressive increase in the damage level with increasing fluence, which is consistent with the behavior of strain shown in Fig. 3(a). Previous studies of irradiated SiC [12, 22, 24] have revealed that the DW factor could be directly interpreted, for a given reflection, in terms of the volume fraction of amorphized or heavily disordered material. The reason for this is that, as shown by MD simulations [30, 31], upon irradiation, no extended defects are formed, even at moderately elevated temperatures as those used here: only point defects and their clusters are formed, and, hence, no diffuse scattering is observed in diffraction patterns. Therefore, the weakening of the coherent intensity can be straightforwardly ascribed to the formation of amorphous or heavily disordered inclusions and interpreted similarly to the damage fraction commonly determined by RBS/C (see section 4 for a more detailed description).

Figures 3(c) and 3(d) show XRD-derived strain and damage profiles, respectively, for samples irradiated at 100 °C. Note that the fluence range investigated at 100 °C is much larger than for the 25 °C case. The first two fluences analyzed at 100 °C (2.5×10^{14} and 5×10^{14} cm^{-2}) correspond approximately to the first and last fluences investigated at 25 °C (2×10^{14} and 5×10^{14} cm^{-2}). The overall shape of the profiles and their evolution observed for the first two fluences are similar to what we observe at 25 °C, for both strain and damage profiles, the only noticeable difference being that the maximum strain is lowered to 6.5 %. For higher fluences (from 7.5×10^{14} cm^{-2} and above), we observe a clear change in the shape of damage profiles. The lattice starts to amorphize (damage $\rightarrow 1$) in the 290-310 nm depth range, and this region expands along the surface normal with increasing fluence. For the highest fluence studied at 100 °C (2.5×10^{15} cm^{-2}), the amorphized region extends from ~150 nm to ~350 nm below the surface; *i.e.,* it preferentially expands towards the surface. In the amorphized region, the diffraction amplitude vanishes ($DW \rightarrow 0$), so that the corresponding strain (which can only be defined for crystalline regions) is meaningless. For this reason, the strain profiles are truncated when the corresponding damage exceeds a threshold value, which is here chosen equal to 0.98 (this value has been determined from the XRD simulations as the limit above which no modification is visually observed in the fitting).

It must here be emphasized that the fact the lattice strain is undefined in amorphous regions (hence the truncated curves in Fig. 3c) does not imply that these regions are free of strain. In fact, their density being lower [32] than that of the crystalline phase, these regions do indeed exhibit a volumetric swelling as compared to their crystalline counterparts, but the lack of long range order in these regions prevents a reliable XRD-based measurement of this volume change[1]. It must therefore be borne in mind that the strain depth-profiles determined in this work only apply to the crystalline regions.

We finally consider the 200 °C irradiated samples [Figs. 3(e) and 3(f)] for which the fluence range is similar to that used for the 100 °C samples. The strain profile is now markedly different than for 25 and 100 °C cases: profiles at 200 °C are asymmetric with a tail extending towards the surface, the maximum strain is shifted to ~310 nm below the surface, and the level of strain is lowered to 5 % at the highest fluence (which is 5 times that used at 25 °C where a maximum strain level of 7 % is observed). Similar conclusions can be drawn for damage profiles at 200 °C [Fig. 3(f)]: profiles are shifted toward larger depths, amorphization occurs at higher ion fluence (~1.1×10^{15} cm^{-2}) and, contrarily to the 100 °C case, the amorphous region remains confined in the 300-350 nm region, even for the highest fluence used (2.3×10^{15} cm^{-2}). The above descriptions of the strain and damage buildup are discussed in the next section.

4. Discussion

4.1 Strain and damage build-up

For the three temperatures studied, the evolution of the maximum damage and strain (*i.e.*, recorded at ~300 nm below the surface) as a function of ion fluence is displayed in Figs. 4(a) and 4(b), respectively. To allow comparison with other studies, we convert ion fluence expressed in cm^{-2} to displacement per atom (dpa) units according to: Fluence (dpa) = Fluence (cm^{-2}) / 1.15×10^{15} [19]. Figures 4(a) and 4(b) provide clear evidence that, at a given ion fluence, levels of both strain and damage decrease with increasing temperature. In order to get further insight into the amorphization process, both sets of experimental data were fitted with a phenomenological model of damage buildup described in [19]. Simulated curves are presented as solid lines in Figs. 4(a) and 4(b).

---

[1] X-ray based techniques such as Small Angle X-ray Scattering which are sensitive to electron density fluctuations (and for which long-range atomic order isn't required) could be used to characterize amorphous regions.

Briefly, simulations were done with a nucleation-limited model [19], initially developed to analyze RBS/C-derived disorder, in which the disorder parameter is the result of two contributions: one coming from point defects and point defect clusters and the other due to amorphous regions. When XRD-derived damage is used as a gauge for disorder, both contributions have the same meaning as for RBS/C. Being a phenomenological model, it can also be used to model the evolution of strain. In this case, since strain can only be defined for crystalline regions, the second contribution corresponds to the evolution of strain in the remaining crystalline regions when amorphous regions are starting to be formed.

The first contribution (point defect clusters) is described by a simple rate equation with a constant defect production cross-section (σ_{cluster}) and a saturation value (f_{sat}). In the present study, the limited number of data points in the fluence range up to the defect cluster saturation stage makes the determination of reliable values of σ_{cluster} and f_{sat} difficult. Hence, σ_{cluster} was taken from RBS/C measurements [19], and f_{sat} was fixed to 0.6 and 0.78 for the strain and damage parameters, respectively (these values were determined for the 200 °C case and assumed identical for 25 and 100 °C). The contribution of amorphous regions obeys a similar production rate but with an amorphization cross-section having a linear dependence on ion fluence: $\sigma_{\text{amorph}} = \xi_{\text{amorph}}\ \Phi\ \mathrm{H}(\Phi - \Phi_{\text{crit}})$, where H is the Heaviside step function, and Φ_{crit} is the critical fluence above which amorphous clusters start to appear. When the damage level is analyzed, ξ_{amorph} represents an amorphization cross-section constant. When the strain is studied, ξ_{amorph} corresponds to the rate of deformation when amorphous inclusions are beginning to be formed. In addition to these parameters, one can define Φ_{amorph}, the fluence at which full amorphization is reached. Note that this value can be derived from the damage buildup only, not from the strain buildup, and Φ_{amorph} was defined as the fluence for which the damage level reaches 0.98. All the fitting parameters are given in Table II.

Based on the analysis of damage buildup [Fig. 4(a) and Table II], the amorphization fluence Φ_{amorph} increases monotonically with increasing temperature. It doubles from 25 to 200 °C. Concomitantly, the amorphization cross-section constant ξ_{amorph} is reduced by a factor of 2.4 at 100 °C and by a factor of 4.3 at 200 °C compared to the 25 °C case. These results show that (i) dynamic annealing in 3C-SiC is already operational at rather moderate temperatures (~100 °C); *i.e.* the effective defect production rate is reduced, and (ii) this process is very efficient since it considerably delays the amorphization. Meanwhile, although Φ_{crit} is found to be constant between 25 and 100 °C, it increases by a factor of 2.3 at 200 °C. A similar finding was made for electron-irradiated SiC [33, 34] and Si-irradiated SiC [35, 36]. This finding indicates that an increase in irradiation temperature, at least above 100 °C, also delays the point defect saturation stage, and point defect clusters are formed up to larger fluences.

Let us now consider the strain buildup [Fig. 4(b) and Table II]. As mentioned above, the maximum strain decreases with increasing temperature, this decrease being much more pronounced at 200 °C. For instance, the maximum level of strain prior to full amorphization (*i.e.,* at Φ_{amorph}) is 7.5 % at 25 °C and 5.1 % at 200 °C (Table II). These results indicate that the remaining crystalline regions are less strained at higher irradiation temperatures. A similar trend is observed for the amorphization cross-section constant (ξ_{amorph}). More interestingly, for ξ_{amorph}, values obtained for the strain buildup are much lower than those determined for the damage buildup (Table II). This finding suggests that amorphous phase inclusions are more effective in generating damage than strain. This is in agreement with the previously reported conclusion that the relaxation of the strain energy associated with defect clusters is the driving force for the formation of amorphous inclusions [22].

Table II further reveals that, within fitting errors, the critical fluence for amorphization (Φ_{crit}) is the same for both the strain and damage buildup. The fact that Φ_{crit} increases with increasing temperature suggests that both strain and damage are concomitantly affected by the same phenomenon that is the appearance of amorphous phase inclusions in the lattice. Moreover, the strain level at Φ_{crit} is similar (~2%) at the three temperatures studied, which further supports the above conclusion that the onset of amorphization is determined by the overall level of strain (and associated strain energy) in the irradiated crystal.

The following damage buildup scenario can, hence, be proposed. In the first step of the disordering process, at low fluences, point-like defects and small defect clusters are formed. At some critical level of stored elastic energy, corresponding to a lattice strain of ~2%, amorphous inclusions start to form. Such an onset of amorphization is reached at higher fluences with increasing temperature due to dynamic annealing. After the onset of amorphization, the level of strain in the remaining (disordered) crystalline regions keeps increasing with increasing fluence. However, the maximum level of strain prior to full lattice amorphization decreases with increasing temperature. Hence, amorphization at higher temperatures requires lower effective concentrations of stable defect clusters since the level of strain reflects the defect concentration, as we discuss in detail in the following section.

4.2 Defect concentrations

In order to go further in this scenario, one can try to quantify defect concentrations. Results of previous MD modeling have suggested that stable radiation damage in SiC mainly consists of small isolated point defect clusters containing few (3 to 5) individuals [9, 11]. In other words, extended defects like Frank loops or voids are not readily formed in the temperature range studied here. This is also clearly illustrated in the review article of Snead *et al.* [3] and confirmed by the lack of diffuse scattering in XRD measurements [12]. In such a case, there is a straightforward relationship between the XRD-measured strain and the concentration of defects in the crystal. For a (001) oriented crystal, the measured strain is connected to the free swelling via [37]:

$$e_{zz}=\frac{\Delta v}{3v}\left(1+2\frac{C_{12}}{C_{11}}\right) \quad , \tag{5}$$

where $\Delta v/v$ is the free swelling of the unit-cell induced by the presence of defects. The second term of the right hand side of Eq. (5) comes from the fact that the damaged layer is formed on a rigid substrate and, hence, is not free to expand laterally; there is, therefore, an additional contribution to the measured strain due to Poisson's expansion. For SiC, we have C_{11} = 449 GPa and C_{12} = 146 GPa [38]. The free swelling is proportional to the defect concentration [39], and, for irradiated SiC, it can be written as:

$$\frac{\Delta v}{v}=\sum_{i=Si,C} c_{V(i)}\frac{v_{V(i)}^{rel}}{\Omega_i}+c_{I(i)}\frac{v_{I(i)}^{rel}}{\Omega_i}+c_{AS(i)}\frac{v_{AS(i)}^{rel}}{\Omega_i} \quad , \tag{6}$$

where c, v^{rel}, and Ω are the atomic concentration for each defect (vacancy: V; interstitial: I; and antisite: AS), the defect relaxation volume, and the atomic volume, respectively.

We here only consider the presence of Frenkel pair (FP) defects (*i.e.,* I/V pairs) and AS defects as those appear to be the main defects formed in irradiated SiC in the temperature range below ~200 °C, as suggested by several previous theoretical studies [40, 41]. As small defect clusters are also present [30, 31, 40, 41], it is here assumed that the volume change Δv of a cluster is proportional to the number of point defects it contains, which is a reasonable assumption for small, non-interacting clusters [42]. It can be seen from Eq. (6) that, if the atomic and relaxation volumes are constant for a given type of defects (which is most likely in the current temperature range), any change in the strain is an indication of a change in the defect concentration.

In order to compute defect concentrations, however, the relative amount of each type of defects is needed. This information can be obtained from collision cascade simulations by MD. For instance, such calculations have been performed in SiC for primary knock-on atoms (PKAs) of different energies, from 0.25 to 50 keV [40, 41], and a comprehensive defect statistics was provided. In the present work, the median PKA energy $T_{1/2}$ was determined from SRIM simulations, and a value of ~6.5 keV was found (considering both Si and C PKAs). Note that it has been shown that the difference in defects (a sum of FP and AS) between C and Si PKA is only about 10 to 20 % [41], so that the same PKA energy can be used for these two elements. By analyzing the data contained in Ref. [40, 41], it appears that, for the present irradiation conditions, the contribution of each type of defects (*i.e.,* Frenkel and AS pairs) is the following: there are 5 times more carbon FP than silicon FP, and AS defects represent 10% of the total defects. Eq.(6) then becomes:

$$\frac{\Delta v}{v}=c_{\mathrm{def}}\left\{w_{FP(Si)}\left[\frac{v_{V(Si)}^{rel}}{\Omega_{Si}}+\frac{v_{I(Si)}^{rel}}{\Omega_{Si}}\right]+w_{FP(C)}\left[\frac{v_{V(C)}^{rel}}{\Omega_{C}}+\frac{v_{I(C)}^{rel}}{\Omega_{C}}\right]+w_{AS}\left[\frac{v_{C(Si)}^{rel}}{\Omega_{Si}}+\frac{v_{Si(C)}^{rel}}{\Omega_{C}}\right]\right\} \quad , \qquad (7)$$

where $w_{\mathrm{FP(Si)}} = 0.15$, $w_{\mathrm{FP(C)}} = 0.75$, $w_{\mathrm{AS}} = 0.1$, and c_{def} is the total concentration of defects: $c_{\mathrm{def}} = c_{\mathrm{V(Si)}} + c_{\mathrm{I(Si)}} + c_{\mathrm{V(C)}} + c_{\mathrm{I(C)}} + c_{\mathrm{AS}} = c_{\mathrm{FP(Si)}} + c_{\mathrm{FP(C)}} + c_{\mathrm{AS}}$. The relaxation volumes corresponding to each defect have been computed by MD [43] and are recalled in Table III together with the associated volume swelling (v^{rel}/Ω). As far as the atomic volume is concerned, using the atomic covalent radius would yield erroneous results as the actual atomic volume is strongly dependent on the number and the nature of the bonds. We, therefore, used the average lattice site volume in SiC; *i.e.,* $\Omega = 10.353\ 10^{-30}$ m^3. The assumptions performed in the calculations, in particular regarding the relative amount of each type of defects, prohibits any possibility of an absolute determination of defect concentrations from the observed strain. Nonetheless, the values obtained should provide reasonable orders of magnitude. Moreover, to our knowledge, there exists no reported quantitative information in the literature regarding irradiation-induced defect concentrations in SiC. Hence, the present approach is interesting by itself and for, *e.g.*, validating atomistic and Monte Carlo simulations.

We used Eq. (5) and (7) to compute the total defect concentration at the maximum strain. Figure 4(b) shows results, revealing defect concentrations that vary from ~1 to ~7 %. Before full amorphization, the defect production rate can be estimated from the slope of the c_{def} *vs.* fluence curve (Fig. 4). For fluences $\Phi < \Phi_{amorph}$, *i.e.* in the 0.2-0.4 range for RT and 100°C and 0.3-1 range for 200°C, this rate is 0.23, 0.19, and 0.044 dpa^{-1} for RT, 100°C, and 200°C, respectively. This is a clear indication of the above-mentioned dynamic annealing process and is in very good agreement with kinetic Monte-Carlo simulations that demonstrated that an enhanced defect recombination occurs for temperatures higher than ~120 °C [11].

Similarly to what is observed for the strain, there is a decrease in the maximum defect concentration with increasing temperature. Before full amorphization, *i.e.* at $\Phi \sim \Phi_{amorph}$, the concentration reduces from 7.3 % to 6.9 % between 25 and 100 °C, and to 5 % at 200 °C. These decreases correspond to ~5 % and ~28 % drops, respectively, which is quite significant. Indeed, for instance, in MgO, another ceramic material for which the same methodology was applied, the decrease in defect concentration from 25 to 300 °C (*i.e.,* more than the 200 °C temperature used here) was only about 13 % [44], and defect mobility is known to be high in MgO (see references in [44]). As mentioned above, since the level of strain within amorphous pockets is not included in our XRD-based measurement of the strain, the net result is a decrease of lattice strain (hence, of the defect concentration) in the remaining crystalline regions at temperatures above RT. This result indicate that at higher temperatures, and for fluences $\Phi \sim \Phi_{amorph}$, enhanced defect migration from the crystalline to the amorphous phase occurs, *i.e.* amorphous pockets act as defect sinks.

Beyond providing quantitative data regarding irradiation-induced defects in SiC, these results can also be used to interpret the change in shape and in peak location in strain profiles with increasing temperature (Fig. 3). As mentioned in above, with increasing temperature, the maximum of the strain profile slightly shifts toward greater depths, and concomitantly a tail spreading toward the surface is observed. These features are clearly visible by comparing strain profiles of Figs. 3(a) and 3(e). In Fig. 4(d) we plot the strain profile and defect concentration observed close to the surface (100 nm below the surface). At the maximum fluence of ~2 dpa, the defect concentration at 100 nm is reduced from 4.9 % (at 100 °C) to 2% (at 200 °C). This represents a reduction of 60 %, which is twice as large compared to the temperature-dependent behavior of the defect concentration at the strain peak (located at ~300 nm below the surface). This result reflects a qualitative change in damage buildup in 3C-SiC at temperatures above 200 °C when amorphization nucleates at the ion end of range region and remains confined there for the entire fluence range used in the present study [see Fig. 3(f) and the discussion in Sec. 4.2]. This is also evident from the evolution of damage observed at 100 nm, Fig. 4(c). Because of the uncertainty in the determination of this parameter induced by the irregularities of the profiles, we plot the average of the damage observed in the 50-150 nm region. The evolution, albeit being relatively noisy, clearly reveals that the region close to the surface is characterized by a damage of 0.55 at 200 °C, whereas full amorphization is observed at 100 °C.

5. Conclusion

The damage accumulation process in 3C-SiC single-crystals irradiated with 500 keV Ar ions at moderately elevated temperatures in the range of 25-200 °C has been investigated by X-ray diffraction experiments combined with an advanced data fitting procedure. Both strain and damage depth profiles have been obtained as a function of ion fluence and temperature. Examination of these profiles provides clear evidence of an increased defect recombination with increasing temperature. More interestingly, the amorphization process is shown to be correlated with the evolution of lattice strain. First, at fluences corresponding to the onset of amorphization, lattice strain is ~2 % irrespective of temperature, which suggests the existence of a threshold stored elastic energy that must be overcome to initiate the formation of amorphous inclusions. Second, with further irradiation above the onset of amorphization, the strain in the crystal bulk keeps on increasing to eventually reach a saturation value that decreases with increasing temperature (from 7% to 5%). In addition, from the strain values, we have computed the effective concentration of point defect clusters and we demonstrated that bombardment at higher temperatures results in lower defect concentrations, hence, providing clear evidence for enhanced defect mobility and defect recombination.

Acknowledgments

Work at LLNL was funded by the Nuclear Energy Enabling Technology (NEET) Program of the U.S. DOE, Office of Nuclear Energy and performed under the auspices of the U.S. DOE by LLNL under Contract DE-AC52-07NA27344. J.B.W would like to acknowledge the LGSP for funding.

References

[1] A. Fissel, Artificially layered heteropolytypic structures based on SiC polytypes: molecular beam epitaxy, characterization and properties, Phys. Rep. 379, 149 (2003)

[2] M. Willander, M. Friesel, Q. Wahab, B. Straumal, Silicon carbide and diamond for high temperature device applications, J. Mater. Sci.: Mater. Electron. 17, 1 (2006)

[3] L. L. Snead, T. Nozawa, Y. Katoh, T. S. Byun, S. Kondo, D. A. Petti, Handbook of SiC properties for fuel performance modeling, J. Nucl. Mater. 371, 329 (2007).

[4] Y. Katoh, L. L. Snead, I. Szlufarska, W. J. Weber, Radiation effects in SiC for nuclear structural applications, Curr. Opin. Solid State Mater. Sci. 16, 143, (2012).

[5] H. Inui, H. Mori, T. Sakata, High-resolution electron microscopy study of electron-irradiation-induced crystalline-to-amorphous transition in α-SiC single crystals, Philos. Mag. B 66, 737 (1992).

[6] C. J. McHargue, J. M. Williams, Ion implantation effects in silicon carbide, Nucl. Inst. Meth. Phys. Res. B 280, 889 (1993).

[7] E. Wendler, A. Heft, W. Wesch, Ion-beam induced damage and annealing behaviour in SiC, Nucl. Inst. Meth. Phys. Res. B 141 (1998) 105.

[8] W. J. Weber, N. Yu, L. M. Wang, Irradiation-induced amorphization in β-SiC, J. Nucl. Mater. 253, 53 (1998)

[9] F. Gao, W. J. Weber, Cascade overlap and amorphization in 3 C− SiC: Defect accumulation, topological features, and disordering, Phys. Rev. B 66, 024106 (2002).

[10] W. Jiang, Y. Zhang, W. J. Weber, Temperature dependence of disorder accumulation and amorphization in Au-ion-irradiated 6 H− Si C, Phys. Rev. B 70, 165208 (2004).

[11] Z. Rong, F. Gao, W. J. Weber, G. Hobler, Monte Carlo simulations of defect recovery within a 10 keV collision cascade in 3C–SiC, J. Appl. Phys. 102, 103508 (2007)

[12] A. Debelle, L. Thomé, D. Dompoint, A. Boulle, F. Garrido, J. Jagielski, D. Chaussende, Characterization and modelling of the ion-irradiation induced disorder in 6H-SiC and 3C-SiC

single crystals, J. Phys. D.: Appl. Phys. 43, 455408 (2010)

[13] N. Swaminathan, D. Morgan, I. Szlufarska, Ab initio based rate theory model of radiation induced amorphization in β-SiC, J. Nucl. Mater. 414, 431 (2011)

[14] C. Jiang, M. J. Zheng, D. Morgan, I. Szlufarska, Amorphization driven by defect-induced mechanical instability, Phys. Rev. Lett. 111, 155501 (2013)

[15] J. Wiktor, X. Kerbiriou, G. Jomard, S. Esnouf, M. -F. Barthe, M. Bertolus, Positron annihilation spectroscopy investigation of vacancy clusters in silicon carbide: Combining experiments and electronic structure calculations, Phys. Rev. B 89, 155203 (2014)

[16] L. L. Snead, Y. Katoh, T. Koyanagi, K. Terrani, E. D. Specht, Dimensional isotropy of 6H and 3C SiC under neutron irradiation, J. Nucl. Mater. 471, 92 (2016).

[17] S. Leclerc, A. Declémy, M. F. Beaufort, C. Tromas, and J. F. Barbot, Evolution of defects upon annealing in He-implanted 4 H-SiC, J. Appl. Phys **98**, 113506 (2005)

[18] J. -F. Barbot, A. Declémy, M. -F. Beaufort, Damage accumulation in He implanted SiC at different temperatures, Phys. Stat. Sol. (a) 210, 218 (2013)

[19] J. B. Wallace, L. B. Bayu Aji, T. T. Li, L. Shao, S. O. Kucheyev, Damage buildup in Ar-ion-irradiated 3C-SiC at elevated temperatures , J. Appl. Phys. 118, 105705 (2015).

[20] J. B. Wallace, L. B. Bayu Aji, L. Shao, S. O. Kucheyev, Time constant of defect relaxation in ion-irradiated 3 C-SiC, Appl. Phys. Lett. 106, 202102 (2015).

[21] L. B. Bayu Aji, J. B. Wallace, L. Shao, S. O. Kucheyev, Non-monotonic temperature dependence of radiation defect dynamics in silicon carbide, Scientific Rep. 6, 30931 (2016).

[22] A. Debelle, A. Boulle, A. Chartier, F. Gao, W. J. Weber, Interplay between atomic disorder, lattice swelling, and defect energy in ion-irradiation-induced amorphization of SiC, Phys. Rev. B 90, 174112 (2014).

[23] A. Boulle, A. Debelle, Strain-profile determination in ion-implanted single crystals using generalized simulated annealing, J. Appl. Cryst. 43, 1046 (2010).

[24] A. Boulle, A. Debelle, Statistical Nature of Atomic Disorder in Irradiated Crystals, Phys. Rev.

Lett. 116, 245501 (2016).

[25] M. Souilah, A. Boulle, A. Debelle, RaDMaX: a graphical program for the determination of strain and damage profiles in irradiated crystals, J. Appl. Cryst. 49, 311 (2016). See also http://aboulle.github.io/RaDMaX/

[26] U. Pietsch, V. Holy, T. Baumbach, High-resolution X-ray scattering – From thin films to lateral nanostructures, Springer-Verlag New York, LLC (2004).

[27] H. Nagasawa, K. Yagi, T. Kawahara, N. Hatta, Reducing Planar Defects in 3C–SiC, Chem. Vap. Deposition 12, 502 (2006).

[28] A. Boulle, D. Chaussende, L. Latu-Romain, F. Conchon, O. Masson, R. Guinebretière, X-ray diffuse scattering from stacking faults in thick 3 C-Si C single crystals, Appl. Phys. Lett. 89, 091902 (2006).

[29] A. Boulle, D. Dompoint, I. Galben-Sandulache, D. Chaussende, Polytypic transformations in SiC: Diffuse x-ray scattering and Monte Carlo simulations, Phys. Rev. B 88, 024103 (2013).

[30] D. E. Farrell, N. Bernstein, W. K. Liu, Thermal effects in 10 keV Si PKA cascades in 3C–SiC, J. Nucl. Mater. 385, 572 (2009)

[31] J. Xi, P, Zhang, C, He, M, Zheng, H, Zang, D, Guo, L. Ma, Evolution of Defects and Defect Clusters in β-SiC Irradiated at High Temperature, Fusion Science and Technology 66, 235 (2014)

[32] X. Kerbiriou, J.-M. Costantini, M. Sauzay, S. Sorieul, L. Thomé, J. Jagielski, J.-J. Grob, Amorphization and dynamic annealing of hexagonal SiC upon heavy-ion irradiation: Effects on swelling and mechanical properties, J. Appl. Phys. 105, 073513 (2009)

[33] H. Inui , H. Mori, H. Fujita, Electron-irradiation-induced crystalline to amorphous transition in α-Sic single crystals, Philos. Mag. B 61, 107 (1990).

[34] H. Inui, H. Mori , A. Suzuki, & H. Fujita, Electron-irradiation-induced crystalline-to-amorphous transition in β-SiC single crystals, Philos. Mag. B 65, 1 (1992).

[35] S.J. Zinkle, L.L. Snead, Influence of irradiation spectrum and implanted ions on the

amorphization of ceramics, Nucl. Instr. Meth. B 116, 92 (1996).

[36] L.L. Snead, S.J. Zinkle, J.C. Hay, M.C. Osborne, Amorphization of SiC under ion and neutron irradiation, Nucl. Instr. Meth. B 141, 123 (1998).

[37] A. Debelle, A. Declémy, XRD investigation of the strain/stress state of ion-irradiated crystals, Nucl. Instrum. Methods B 268, 1460 (2010).

[38] F. Gao, W. J. Weber, Mechanical properties and elastic constants due to damage accumulation and amorphization in SiC, Phys. Rev. B 69, 224108 (2004)

[39] P. Ehrhart, Investigation of radiation damage by X-ray diffraction, J. Nucl. Mater. 216, 170 (1994).

[40] F. Gao, W.J. Weber, R. Devanathan, Defect production, multiple ion–solid interactions and amorphization in SiC, Nucl. Instr. Methods. B 191, 487 (2002)

[41] R. Devanathan, W. J. Weber and F. Gao, Atomic scale simulation of defect production in irradiated 3C-SiC, J. Appl. Phys. 90, 303 (2001)

[42] P. H. Dederichs, Effect of Defect Clustering on Anomalous X-Ray Transmission, Phys. Rev. B 1, 1306 (1970).

[43] J. Li, L. Porter, S. Yip, Atomistic modeling of finite-temperature properties of crystalline β-SiC: II. Thermal conductivity and effects of point defects, J. Nucl. Mater. 255, 139 (1998)

[44] D. Bachiller-Perea, A. Debelle, L. Thomé, J. -P. Crocombette, Study of the initial stages of defect generation in ion-irradiated MgO at elevated temperatures using high-resolution X-ray diffraction, J. Mater. Sci. 51, 1456 (2016)

Table I. Ion fluences used for each sample

Irradiation temperature	Ion fluence (cm^{-2})
RT	2×10^{14} ; 3×10^{14}; 3.5×10^{14}; 4×10^{14}; 5×10^{14}
100 °C	2.5×10^{14}; 5×10^{14}; 7.5×10^{14}; 1×10^{15}; 1.25×10^{15}; 1.5×10^{15}; 2×10^{15}; 2.5×10^{15}
200 °C	1×10^{14}; 3×10^{14}; 5×10^{14}; 7×10^{14}; 1.1×10^{15}; 2.3×10^{15}

Table II. Evolution with temperature of the parameters of the strain/damage kinetics. See text for definitions.

	Strain			Damage		
T (°C)	Max. strain (%)	ξ_{amorph} (dpa^{-2})	Φ_{crit} (dpa)	Φ_{amorph} (dpa)	ξ_{amorph} (dpa^{-2})	Φ_{crit} (dpa)
25	7.5±0.1	28±1	0.17±0.01	0.37±0.01	60±4	0.17±0.01
100	7.1±0.1	24±2	0.20±0.02	0.51±0.02	25±2	0.18±0.02
200	5.1±0.1	4±1	0.44±0.02	0.74±0.02	14±2	0.42±0.02

Table III. Relaxation volumes of defects in SiC. V(Si) and V(C) are Si and C vacancies, respectively. I(Si)$_{Si}$ and I(Si)$_C$ are Si interstitials in Si or C tetrahedral environment, respectively. Both are assumed equiprobable, and we use the average value <I(Si)>. Similar definitions hold for C interstitials. Si(C) (respectively C(Si)) is an isolated Si (respectively C) antisite (AS) defect, and Si(C)+C(Si) corresponds to a close AS defect pair. Isolated and close AS defects are assumed equiprobable, and the average value is used. Bold values indicate those used in Eq.(7).

Defect	V(Si)	V(C)	I(Si)$_{Si}$	I(Si)$_C$	<I(Si)>	I(C)$_{Si}$	I(C)$_C$	<I(C)>	Si(C)	C(Si)	Si(C)+ C(Si)	<AS>
Relaxation volume, v^{rel} (10^{-30} m^3)	**1.85**	**2.68**	27.88	37.22	**32.55**	16.48	15.33	**15.905**	15.44	-9.52	3.88	**4.9**
Volumic swelling, v^{rel} / Ω	**0.179**	**0.259**	2.693	3.595	**3.144**	1.592	1.481	**1.536**	1.491	-0.92	0.375	**0.22**

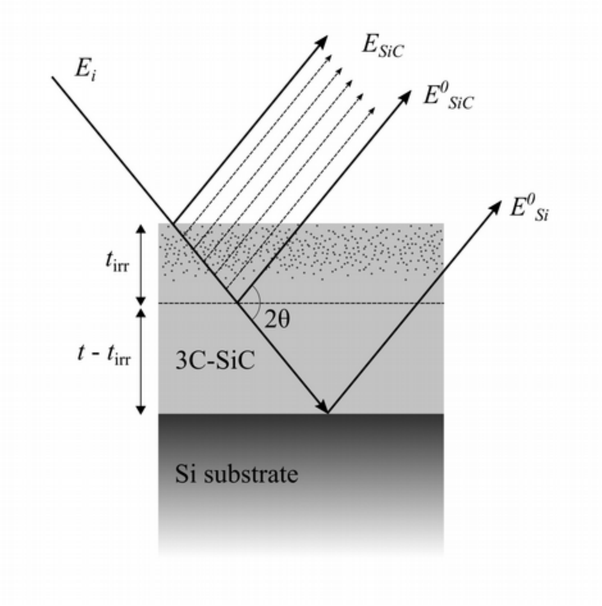

Fig. 1. Schematic representation of the diffraction geometry. The irradiated region (thickness t_{irr}) is divided into lamellas in order to compute the corresponding amplitude E_{SiC}. The underlying pristine SiC (thickness t - t_{irr}) and Si have amplitudes of $E^0{}_{\mathrm{SiC}}$ and $E^0{}_{\mathrm{Si}}$, respectively. 2θ is the diffraction angle. E_{i} is the amplitude of the incident beam.

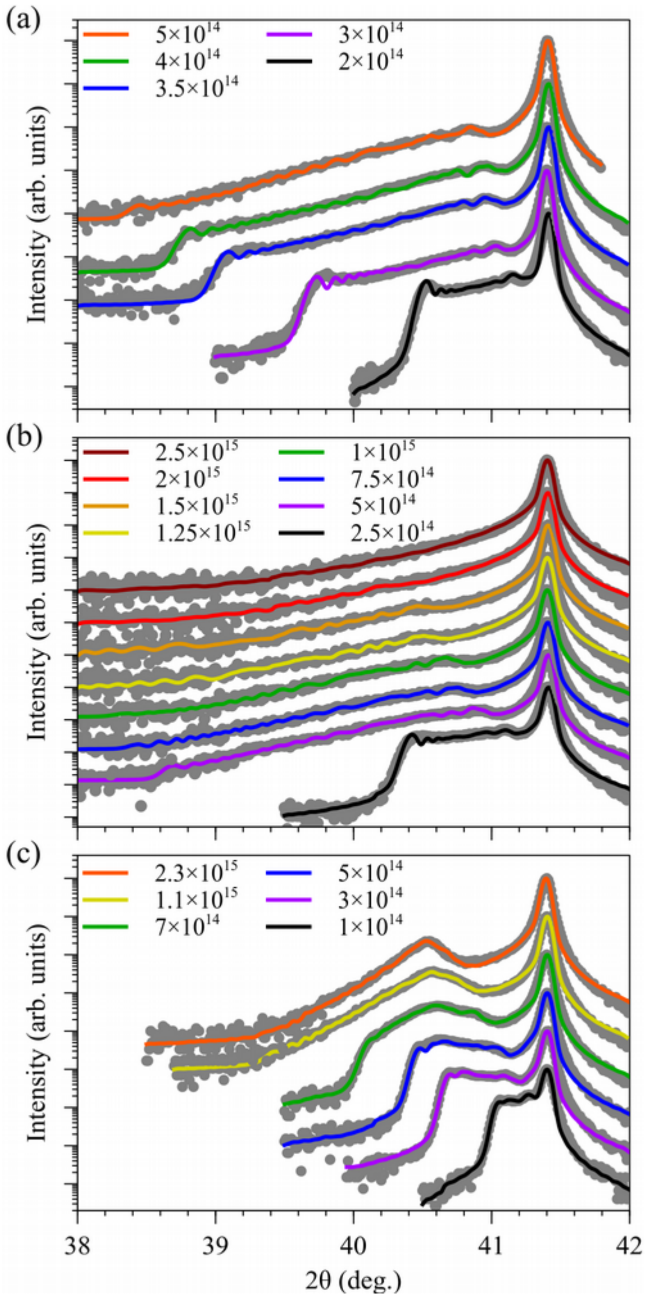

Fig. 2. Evolution with increasing ion fluence of the 002 peak in XRD profiles of 3C-SiC irradiated at (a) 25, (b) 100, and (c) 200 °C with 500 keV Ar ions. Symbols are experimental data, while lines are results of simulations described in the text.

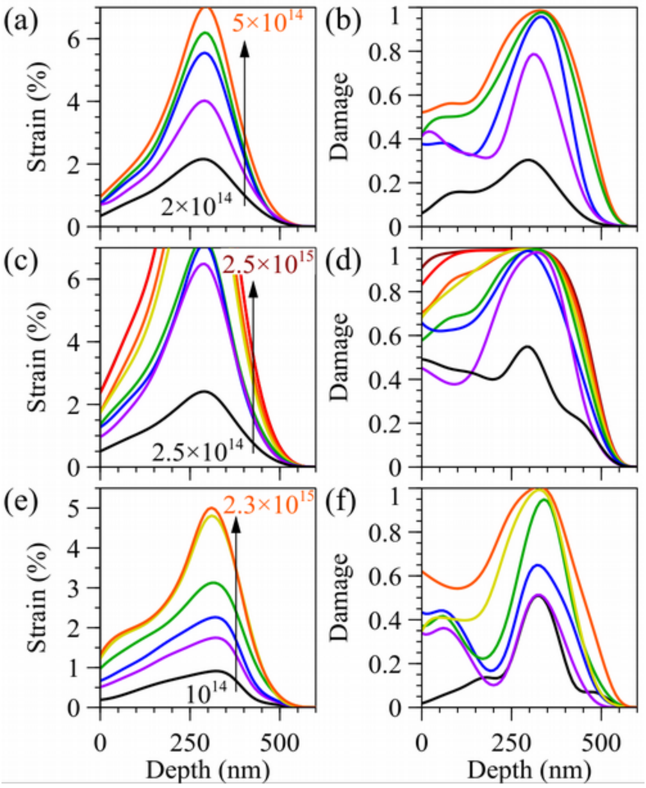

Fig. 3. Evolution with increasing fluence of the XRD-retrieved depth profiles of [(a), (c), and (e)] strain and [(b), (d), and (f)] damage for 3C-SiC irradiated at [(a), (b)] 25 °C, [(c), (d)] 100 °C, and [(e), (f)] 200 °C with 500 keV Ar ions. The same color scheme as in Fig. 1 is used for increasing fluence.

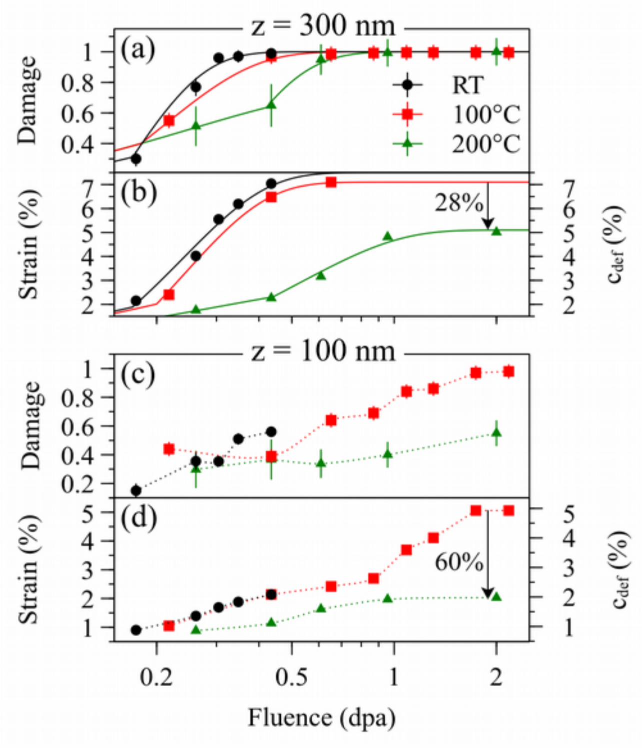

Fig. 4. Evolution with increasing fluence of the damage and strain observed [(a), (b)] at the damage peak (*i.e.*, at 300 nm below the surface) and [(c), (d)] at 100 nm below the surface. Symbols are experimental data, while continuous lines in (a, b) are results of fitting with a stimulated amorphization model described in the text. Dotted lines are guides to the eye (c, d). The right axis is defect concentration computed with Eq. (7).